

# High-resolution imaging of the evolving bipolar outflows in symbiotic novae: the case of RS Ophiuchi 2021 nova outburst

R. Lico<sup>1,2,\*</sup>, M. Giroletti<sup>1</sup>, U. Munari<sup>3</sup>, T. J. O'Brien<sup>4</sup>, B. Marcote<sup>5,6</sup>, D. R. A. Williams<sup>4</sup>, J. Yang<sup>7</sup>, P. Veres<sup>8</sup>, and P. Woudt<sup>9</sup>.

<sup>1</sup> INAF Istituto di Radioastronomia, via Gobetti 101, 40129 Bologna, Italy.

<sup>2</sup> Instituto de Astrofísica de Andalucía-CSIC, Glorieta de la Astronomía s/n, 18008 Granada, Spain.

<sup>3</sup> INAF Osservatorio Astronomico di Padova, 36012 Asiago, VI, Italy.

<sup>4</sup> Jodrell Bank Centre for Astrophysics, School of Physics and Astronomy, University of Manchester, Manchester M13 9PL, UK.

<sup>5</sup> Joint Institute for VLBI ERIC, Oude Hoogeveensedijk 4, 7991 PD Dwingeloo, The Netherlands.

<sup>6</sup> ASTRON, Oude Hoogeveensedijk 4, 7991 PD Dwingeloo, The Netherlands.

<sup>7</sup> Dept. of Space, Earth and Environment, Chalmers University of Technology, Onsala Space Observatory, 43992 Onsala, Sweden.

<sup>8</sup> Center for Space Plasma and Aeronomic Research (CSPAR), University of Alabama in Huntsville, Huntsville, AL 35899, USA.

<sup>9</sup> Department of Astronomy University of Cape Town, Private Bag X3, Rondebosch 7701, South Africa.

Received February xx, 2024; accepted xx

## ABSTRACT

**Context.** The recurrent and symbiotic nova RS Ophiuchi (RS Oph) underwent a new outburst phase during August 2021, about 15 years after the last event occurred in 2006. This represents the first nova event ever detected at very-high energies (VHE,  $E > 100$  GeV), and a whole set of coordinated multi-wavelength observations were triggered.

**Aims.** The main goals of this work are to characterize the evolving morphology of the expanding bipolar ejecta with high accuracy and determine the physical conditions of the surrounding medium in which they propagate.

**Methods.** By means of high-resolution very long baseline interferometry (VLBI) radio observations, we monitored RS Oph with the European VLBI Network (EVN) and e-MERLIN at 1.6 and 5 GHz during multiple epochs from 14 to 65 days after the explosion.

**Results.** We reveal an evolving source structure, consisting of a central and compact core and two elongated bipolar outflows, expanding on opposite sides from the core in east-west direction. The ejecta angular separation with time is consistent with a linear expansion with an average speed of  $\sim 7000$  km s<sup>-1</sup>. We find clear evidence of a radial dependence of the density along the density enhancement on the orbital plane (DEOP), going from  $1.1 \times 10^7$  cm<sup>-3</sup> close to the central binary to  $3.8 \times 10^5$  cm<sup>-3</sup> at  $\sim 175$  AU.

**Conclusions.** Thanks to the accurate source astrometric position provided by *Gaia* DR3, in this work we draw a detailed scenario of the geometry and physics of the RS Oph evolving source structure after the most recent nova event. We conclude that most of the mass lost by the red giant companion goes in the DEOP, for which we estimate a total mass of  $4.3 \times 10^{-6} M_{\odot}$ , and in the circumstellar region, while only a small fraction (about one-tenth) is accreted by the white dwarf.

**Key words.** novae – cataclysmic variables – stars: winds, outflows

## 1. Introduction

RS Ophiuchi (hereafter RS Oph) is a well-known recurrent and symbiotic nova, located at  $2.68 \pm 0.17$  kpc distance according to *Gaia* DR3 parallax (Gaia Collaboration et al. 2016, 2023). It consists of a massive white dwarf (WD) and a M0III red giant (RG) in a close binary system with an orbital period of  $\sim 454$  days (Brandi et al. 2009). Before accumulating on its surface, the material accreted from the RG by the WD flows through a massive accretion disk. The near-Chandrasekhar mass of the WD coupled with its large accretion-rate fit with theoretical expectations of a nova outburst every  $\sim 20$  yrs (cf. Nelson et al. 2011), and at least seven eruptions have been already recorded from RS Oph, in 1898, 1933, 1958, 1967, 1985, 2006, and 2021. All these events have evolved nearly identically at optical wavelengths. During an outburst of RS Oph, most of the accreted material is ejected ( $\sim 10^{-6} M_{\odot}$ ; Das et al. 2006; Eyres et al. 2009; Pandey et al. 2022) at high velocity ( $V_{ej} \geq 7500$  km s<sup>-1</sup>; Munari et al. 2022), and the amount of accreted mass retained on the

surface of the WD is sufficient to support stable nuclear burning for about three months (Osborne et al. 2011; Page et al. 2022; Munari & Valisa 2022). The accretion disk is destroyed away by the nova ejecta, and it takes  $\sim 260$  days for it to reform and return to pre-outburst brightness (Zamanov et al. 2022; Munari & Tabacco 2022), marking the start of a new accretion cycle leading to the next outburst.

During August 2021, RS Oph underwent a new eruption that has been the first nova outburst ever detected at the very-high energies ( $E > 100$  GeV) mapped by Cherenkov telescopes (H.E.S.S. Collaboration et al. 2022; Acciari et al. 2022). Prompt observations as well as monitoring campaigns were triggered throughout electromagnetic spectrum, including radio (Sokolovsky et al. 2021; Williams et al. 2021; de Ruiter et al. 2023; Nayana et al. 2024), infrared (Woodward et al. 2021), optical (Munari & Valisa 2021, 2022; Azzollini et al. 2023; Molaro et al. 2023; Tomov et al. 2023), X-ray (Shidatsu et al. 2021; Page et al. 2022; Orio et al. 2023; Ness et al. 2023; Islam et al. 2024), and  $\gamma$ -rays (Cheung et al. 2022). The interpretation of the data thus gathered has particularly benefited from the fact that simi-

\* Email: rlico@ira.inaf.it

**Table 1.** Details of the observations.

Epoch	Obs. date (2021)	$T - T_0$ (days)	Freq. (GHz)	Restoring beam (mas $\times$ mas, $^\circ$ )	Map peak mJy/beam	$1\sigma$ rms mJy/beam	Stations <sup>a</sup>
I	Aug. 22	14	5	$1.5 \times 4.2$ , 75.9	15.66	0.08	JB1,WB,EF,MC,IR,YS,TR,HH,SH
	Aug. 23	15	1.6	$4.4 \times 18.1$ , 76.3	45.37	0.19	JB1,WB,EF,MC,IR,TR,HH
II	Sep. 1	24	5	$6.9 \times 11.5$ , -5.7	9.58	0.01	JB1,WB,EF,MC,IR,YS,O8,T6
	Sep. 2	15	1.6	$10.4 \times 43.4$ , 10.7	18.32	0.07	JB1,WB,EF,MC,IR,TR,HH,O8,T6
III	Sep. 11	34	5	$1.3 \times 2.8$ , 75.4	3.25	0.03	JB2,WB,EF,MC,IR,YS,TR,HH,SH,O8,SV,ZC,BD,e-MERLIN
	Sep. 12	35	1.6	$9.0 \times 11.9$ , 26.3	6.85	0.06	JB2,WB,EF,MC,IR,TR,HH,O8,T6,SV,ZC,BD,e-MERLIN
IV	Sep. 26	49	5	—	—	—	—
	Sep. 27	50	1.6	—	—	—	—
V	Oct. 11	64	5	$1.3 \times 2.6$ , 71.3	4.50	0.04	JB2,WB,EF,MC,IR,YS,TR,HH,SH,O8,SV,ZC,BD,NT,e-MERLIN
	Oct. 12	65	1.6	$9.9 \times 45.6$ , -1.3	4.56	0.05	JB2,WB,EF,MC,IR,TR,HH,O8,NT,SV,ZC,BD,e-MERLIN

**Notes.**

<sup>(a)</sup> EVN stations: Badary (BD), Effelsberg (EF), Hartebeesthoek (HH), Irbene (IR), Jodrell Bank - Lovell (JB1), Jodrell Bank - Mark2 (JB2), Medicina (MC), Noto (NT), Onsala (O8), Shanghai - 25 m (SH), Tianma - 65 m (T6), Svetloe (SV), Toruń (TR), Yebes (YS), Westerbork (WB), Zelenchukskaya (ZC). e-MERLIN outstations: Cambridge, Darnhall, Defford, Knockin, and Pickmere.

lar instrumentation and observing strategies as used for the 2006 eruption were also adopted in 2021, especially in monitoring the evolution in X-rays (eg. Osborne et al. 2011; Page et al. 2022) and imaging in the radio the expansion of the ejecta (eg. O’Brien et al. 2006; Rupen et al. 2008; Munari et al. 2022; Giroletti et al. 2023). Of special benefit has been the extremely accurate astrometric position and proper motions of RS Oph provided by *Gaia* DR3, as in the case of the recent work on the nova V407 Cygni by Giroletti et al. (2020).

Within this context, we have conducted a multi-frequency and five-epoch very long baseline interferometry (VLBI) monitoring campaign with the European VLBI network (EVN), at 1.6 and 5 GHz, which covered RS Oph from about two weeks (late August) up to two months (early October) after the 2021 explosion. The 5 GHz data for the central epoch (day +34) have already been presented and 3D modeled by Munari et al. (2022) in conjunction with results from high-resolution optical spectroscopy, while a preliminary overlook to the whole set of EVN observations has been provided by Giroletti et al. (2023). In this paper we publish the complete set of results from the full EVN monitoring, that allows us to characterize, with an unprecedented level of detail, the evolving source structure and the physical conditions of the surrounding medium in which the nova ejecta propagated.

Assuming the *Gaia* distance of 2.7 kpc, 1 mas corresponds to 2.7 AU. Throughout the paper the radio spectral index  $\alpha$  is defined as  $S_\nu \propto \nu^\alpha$ , with  $S_\nu$  representing the flux density at frequency  $\nu$ , and all angles are measured from North to East. Finally, we use as the reference epoch  $T_0$  the start of the eruption derived to be 2021 August 08.50 ( $\pm 0.01$ ) UT by Munari & Valisa (2021).

## 2. Observations and data calibration

We monitored RS Oph from 22 August 2021 ( $T_0 + 14$  days) to 12 October 2021 ( $T_0 + 65$  days) with the EVN and e-MERLIN at 1.6 and 5 GHz. The observations were organized in 10 observing sessions, grouped in five epochs, with each epoch consisting of two 8-hour runs on consecutive days at 5 and 1.6 GHz, respectively (see Table1).

The EVN participating stations were: Badary, Effelsberg, Hartebeesthoek, Irbene, Jodrell Bank, Medicina, Noto, Onsala, Shanghai, Svetloe, Torun, Yebes, Westerbork, Zelenchukskaya. The last six observing runs also feature the e-MERLIN outsta-

tions in Cambridge, Darnhall, Defford, Knockin, and Pickmere. Observations were performed in dual polarization mode with a bandwidth of 128 MHz (divided into  $4 \times 32$  MHz-wide sub-bands) at 1.6 GHz and 256 MHz (divided into  $8 \times 32$  MHz-wide sub-bands) at 5 GHz. We used a standard phase-reference observing scheme, with 4 min on the target and 40 seconds on the calibrator J1745-0753.

The data correlation was performed in real time with the software FX-kind correlator (SFXC) at the Joint Institute for VLBI ERIC (JIVE, The Netherlands) (Keimpema et al. 2015). The a-priori data reduction was carried out with the JIVE EVN pipeline based on ParselTongue (Kettenis et al. 2006) and AIPS (Greisen 2003). We used the DIFMAP software package (Shepherd 1997) to inspect and edit the calibrated data downloaded from the EVN Data Archive<sup>1</sup>, as well as for the imaging and self-calibration procedures. In more detail, for the imaging process we used the classical inverse modeling CLEAN algorithm, implemented in the DIFMAP, that represents the source structure as a collection of point sources, whose location and flux densities are iteratively determined (Högbom 1974).

We note that the two observing runs of Epoch IV (26 and 27 September 2021) were strongly affected by a hardware problem with e-MERLIN and were excluded from the analysis presented in this paper. Additional details about the observations can be found in Munari et al. (2022) and Giroletti et al. (2023).

## 3. Results

### 3.1. Images and source structure

In the left panel of Fig. 1 we show the 5 GHz images, obtained for the epochs I, II, III and V (14, 24, 34 and 64 days after  $T_0$ , respectively). All images have been convolved with a beam of  $9.8 \text{ mas} \times 12.8 \text{ mas}$  at 0 deg, resulting from the average beam sizes across all the epochs, and displayed with natural weights and a Gaussian taper of 0.5 at  $10 \text{ M}\lambda$ . The 1.6 GHz images, obtained for the epochs I, II, III and V (15, 25, 35 and 65 days after  $T_0$ , respectively), are reported in the right panel of Fig. 1. All 1.6 GHz images have been convolved with a beam of  $8.5 \text{ mas} \times 30.0 \text{ mas}$  at 0 deg, resulting from the average beam sizes across all the epochs, and displayed with natural weights. All images are centered at the *Gaia* DR3 astrometric position for RS Oph,

<sup>1</sup> <http://archive.jive.nl/scripts/portal.php>

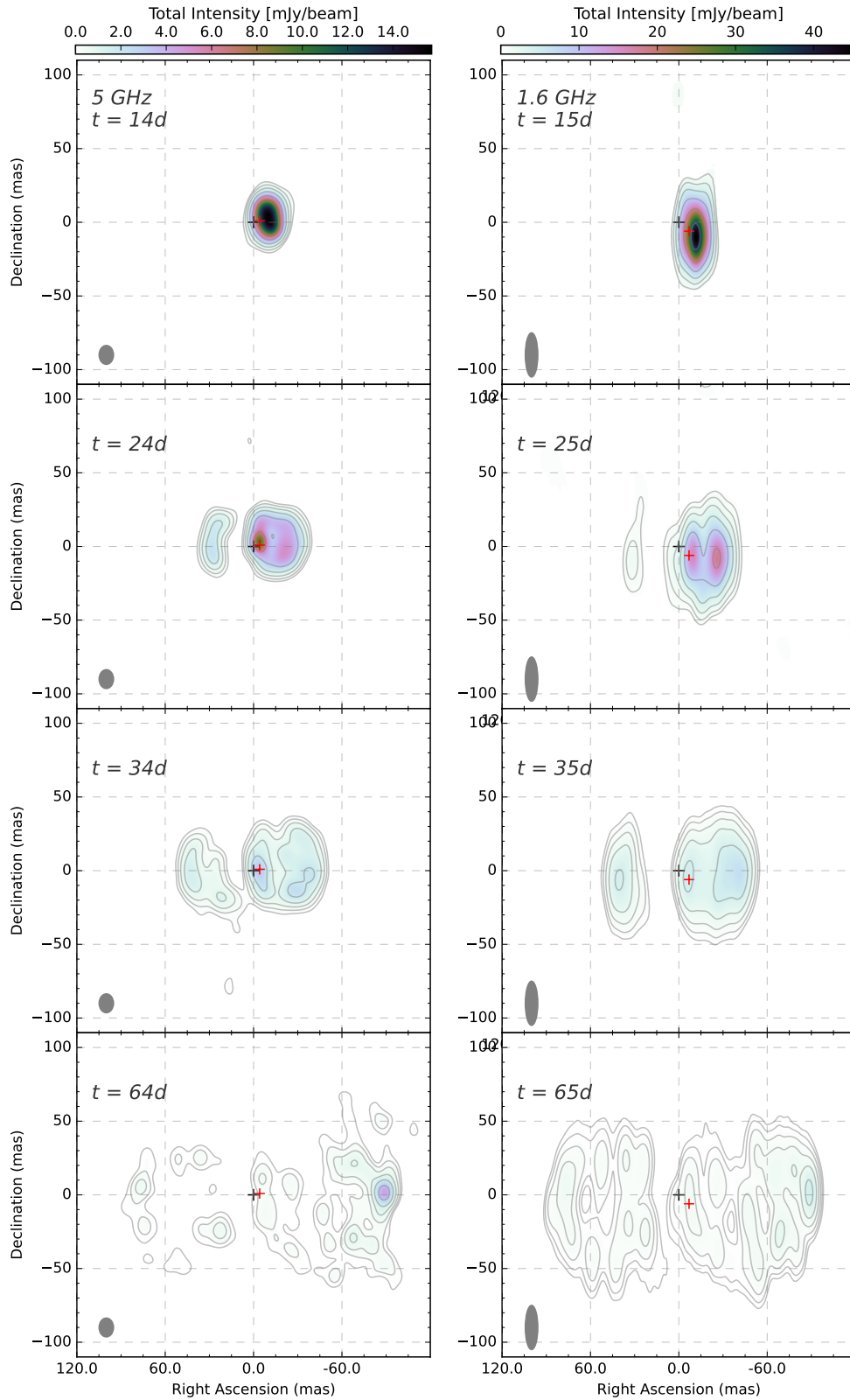


**Fig. 1.** Natural-weighted total intensity images at 5 GHz (left frame) and 1.6 GHz (right frame), centered at the *Gaia* DR3 astrometric position for RS Oph (RA 17h50m13.1610s, Dec  $-06^{\circ}42'28.61026''$ ), corrected for proper motion (indicated by a black cross whose size represents the position uncertainty magnified by a factor of 40 for visualization purpose). The observing epoch, in units of days after  $T_0$ , is indicated in the top-left corner of each image. All 5 GHz images (left panel) are displayed with a Gaussian taper of 0.5 at  $10 \text{ M}\lambda$  and convolved with a beam of  $9.8 \text{ mas} \times 12.8 \text{ mas}$  at  $0^\circ$ . All 1.6 GHz images (right panel) are convolved with a beam of  $8.5 \text{ mas} \times 30.0 \text{ mas}$  at  $0^\circ$ . This restoring beam is displayed in the bottom-left corner in each image. The color scale and the overlaid contours represent the total intensity emission, with the lowest contour at 2% of the map peak (see Table 1) and the following contours a factor of two higher. The red cross indicates the average core position (see Sect. 3.2).

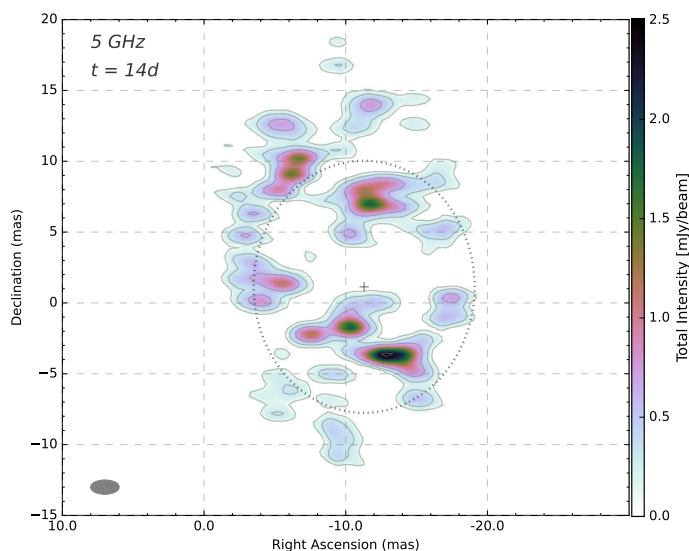


**Fig. 2.** Full resolution 5 GHz total intensity image during epoch I (14 days after  $T_0$ ), with relative coordinates referring to the *Gaia* DR3 astrometric position of RS Oph, corrected for proper motion. The convolving beam, displayed to the bottom-left corner of the image, is  $1.0 \text{ mas} \times 2.0 \text{ mas}$  at  $90^\circ$ . The color scale and the overlaid contours represent the total intensity emission, with the lowest contour at 5% of the map peak (see Table 1) and the following contours a factor of two higher. The gray dots represent the best-fitting ellipse obtained by O’Brien et al. (2008) at the same frequency and epoch after the 2006 outburst.

corrected for proper motion (highlighted with a black cross at the center of each image).

The images at both frequencies reveal an evolving source morphology expanding in the east-west direction, that during the last observing epoch (64–65 days after  $T_0$ ) reaches a total extension of  $\sim 200 \text{ mas}$  ( $\sim 540 \text{ AU}$ ). As it is apparent since epoch II (24–25 days after  $T_0$ ), at both frequencies, the images reveal a triple-component source structure, with a compact central component (core) and two elongated lobe structures propagating on opposite sides from the core. We note that the compact core is located within a few mas from the *Gaia* DR3 position (see Sect. 3.2 for more details). The flux density depression between the eastern lobe and the rest of the source is interpreted by Munari et al. (2022) as due to absorption from ionized gas in the so-called *density enhancement on the orbital plane* (DEOP).

The western lobe is brighter than the eastern one and has a circular shape that is consistent with what was found in the images at similar observing frequencies from the previous 2006 nova event (O’Brien et al. 2006; Rupen et al. 2008). On the other hand, the arc-like structure that we see on the eastern side is assumed to represent the outer edge of the eastern lobe that emerges from behind the DEOP. Within this scenario, we interpret the compact structure that we see during the first epoch (14–15 days from  $T_0$ ), at both frequencies, as the western lobe, with the core in the background and the eastern lobe behind the DEOP.

### 3.1.1. First epoch 5 GHz full-resolution image

To better investigate the structure at the early stages of evolution, we show in Fig. 2 the total intensity image of epoch I (14 days after  $T_0$ ) at 5 GHz in full resolution, centered at the *Gaia* position. The image is obtained adopting uniform weights and a

convolving beam of  $1.0 \text{ mas} \times 2.0 \text{ mas}$  at  $90^\circ$ . The radio emission, which could hardly be resolved in the image obtained with natural weights, is now found to be distributed in a complex and elongated morphology. The total extension is over  $\sim 30 \text{ mas}$  in the north-south direction and  $\sim 20 \text{ mas}$  in the east-west direction. Several spots of enhanced brightness are distributed mostly along the outer rim of this roughly elliptical region. These spots may mark locations of harder collision between the fast ejecta and the pre-existing slow circumstellar material, a situation reminiscent of what Chomiuk et al. (2014) first observed in Nova Mon 2012.

A similar elongated source structure, at the same observing frequency, was reported by O’Brien et al. (2008) with the Very Long Baseline Array (VLBA), 14 days after the 2006 outburst. For comparison, in Fig. 2 we report the best-fit ellipse (gray dots) obtained by O’Brien et al. (2008), with a semi-major axis of  $8.9 \text{ mas}$  and axial ratio of  $1.14 \text{ mas}$ .

### 3.2. Lobe expansion speed

To represent and quantify the emission from the central core, that emerges from the second epoch on, we model the brightness distribution with a 2-D circular Gaussian component in the visibility plane with the `model fit` procedure in DIFMAP. We define a reference core position by averaging the core Gaussian component position during the epochs II and III, when the core region is compact, bright and clearly recognizable at both frequencies. The average core position is indicated in all images in Fig. 1 with a red cross at a distance from the *Gaia* DR3 position of  $\sim 4$  and  $\sim 10 \text{ mas}$  at 5 and 1.6 GHz, respectively. The size of the expanding lobes is determined as the distance of the outermost lowest total intensity contour from the average core position (see Table 2). We note that the orbital separation of RS Oph amounts to  $\sim 1.5 \text{ AU}$  or  $4 \text{ mas}$  at the *GAIA* distance.

By considering the extension of the two lobes from the core region during the different epochs (Fig. 3), and assuming zero separation at  $T_0$ , we obtain their projected expansion speeds by means of a least-squares regression (column 6 in table 2). We note that for the uncertainties on the distance from the core we assume a conservative value equal to the beam minor axis. Since during epoch I (14–15 days after  $T_0$ ) the eastern lobe is not yet visible and we cannot easily disentangle the western lobe from the core region, we do not consider this epoch when estimating the lobe expansion rate.

For the western lobe we obtain an average projected expansion speed of  $6840 \pm 370 \text{ km s}^{-1}$  at 5 GHz and  $6660 \pm 100 \text{ km s}^{-1}$  at 1.6 GHz. For the eastern lobe we obtain an average projected expansion speed of  $6830 \pm 340 \text{ km s}^{-1}$  at 5 GHz and  $7100 \pm 540 \text{ km s}^{-1}$  at 1.6 GHz. The projected expansion velocity of the two lobes is therefore the same well within their combined errors.

### 3.3. Light-curves and spectral index

To quantify the emission from the different source components we use the following approach. We determine the source total flux density by summing up the flux density over all the clean components in DIFMAP, while the core flux density is provided by the 2-D circular Gaussian component that represents the core region (see Sect. 3.1). The eastern lobe can be clearly isolated from the overall source structure and its flux density is obtained by summing up the flux density over all the clean components in this region. Lastly, the western lobe flux density is determined

by subtracting the emission of the eastern lobe and the core from the total flux density.

In Fig. 4 we report the resultant light-curves. The flux density values are reported in table 3, with the uncertainties calculated by considering a calibration error of 10% of the flux density and a statistical error equal to the map rms noise multiplied for number of beams in the area over which the flux density was determined.

The total source emission (first frame in Fig. 4) shows an overall decreasing trend with time, with a  $\sim 50\%$  drop from epoch I ( $\sim 80$  mJy and  $\sim 40$  mJy at 1.6 GHz and 5 GHz, respectively) to Epoch V ( $\sim 40$  mJy and  $\sim 20$  mJy at 1.6 GHz and 5 GHz, respectively). A similar decreasing trend in the flux density with time is also found, at both frequencies, for the core and the western lobe (second and third frame in Fig. 4, respectively). We also note that the western lobe is brighter than both the core and the eastern lobe. On the contrary, for the eastern lobe the flux density tends to increase with time, as the outer part of the lobe itself emerges behind the DEOP (fourth frame in Fig. 4). During the last observing epoch at 1.6 GHz the eastern lobe flux density decreases with respect to the previous two epochs, as the source becomes more diffuse.

The spectral index for the different source components is reported in Fig. 5 and Table 4. The western lobe (green squares) has slightly negative spectral index, with an average value of  $-0.38 \pm 0.12$  across the entire observing period covering about two months after  $T_0$ . The core region (black circles) has an average value of  $-0.50 \pm 0.12$ , until epoch III (34-35 days after  $T_0$ ), and then becomes steeper ( $-1.13 \pm 0.13$ ) during the last epoch (64-65 days from  $T_0$ ). On the other hand, the eastern lobe during epoch II (24-25 days after  $T_0$ ) shows a slightly positive spectral index (blue triangles in Fig. 5) with a value of  $0.10 \pm 0.13$ . In the following epochs, the eastern lobe spectral index follows a similar trend as for the western lobe: it becomes slightly negative during epoch III (34-35 days after  $T_0$ ) to a value of  $-0.39 \pm 0.13$  and later steepens to a value of  $-1.17 \pm 0.14$  during the last epoch (64-65 days from  $T_0$ ). The uncertainties on the spectral index were calculated from the error propagation theory (see Lico et al. 2012).

### 3.4. Core region brightness temperature

For the core region, that we represent by means of 2-D circular Gaussian components across the different epochs (see Sect. 3.2), we estimate the observed brightness temperature ( $T_B^{obs}$ ), by using the following equation (e.g. Tingay et al. 1998):

$$T_B^{obs} = 1.22 \times 10^{12} \frac{S_{core}}{\theta_{maj}\theta_{min}\nu^2} \quad (1)$$

with  $S_{core}$  being the fitted core flux density in Jy,  $\theta_{maj}$  and  $\theta_{min}$  the FWHM of the major and minor axes of the 2-D Gaussian component in mas, and  $\nu$  the observing frequency in GHz. The FWHMs of the Gaussian components during epochs II, III and V are 1.6, 4.2, 12.7 mas at 5 GHz and 4.4, 5.9, 15.5 mas at 1.6 GHz, respectively.

During epoch II (24-25 days after  $T_0$ ), III (34-55 days after  $T_0$ ) and V (64-65 days after  $T_0$ ) we find a brightness temperature of the order of  $7.0 \times 10^7$  K,  $7.8 \times 10^6$  K and  $3.0 \times 10^5$  K at 5 GHz and  $4.0 \times 10^8$  K,  $6.7 \times 10^7$  K and  $4.6 \times 10^6$  at 1.6 GHz, respectively, clearly supporting a non-thermal origin of the radio emission, consistent with spectral index  $< -0.1$ .

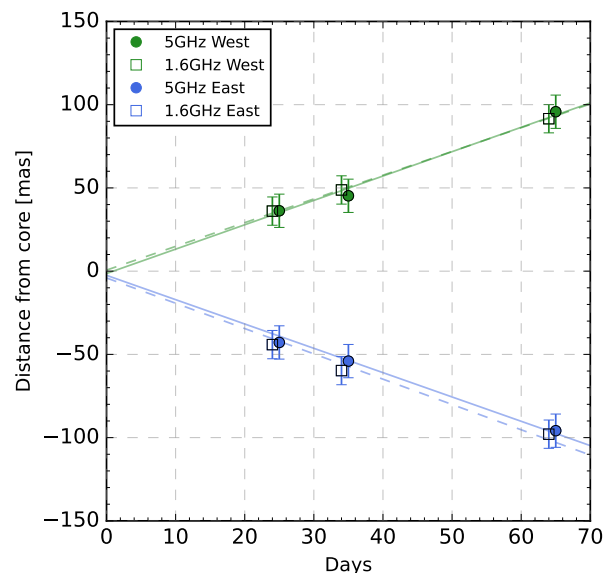


**Fig. 3.** Angular separation evolution with time of the eastern (blue) and the western (green) lobes, at 1.6 GHz (empty squares) and 5 GHz (filled circles). The solid and dashed lines represent the best least-square regression fit for the 5 and 1.6 GHz data, respectively.

**Table 2.** Lobe extension during the different observing epochs (columns 3 - 5) and expansion speed (column 6).

	Lobe	Epoch II	Epoch III	Epoch V	Projected expansion speed
		mas (AU)	mas (AU)	mas (AU)	km s <sup>-1</sup>
5 GHz	West	36.3 (98)	45.3 (122)	95.8 (259)	6840 ± 370
	East	42.8 (116)	54.0 (146)	95.8 (259)	6830 ± 340
1.6 GHz	West	36.1 (97)	48.8 (132)	91.6 (247)	6660 ± 100
	East	44.1 (119)	59.7 (161)	97.9 (264)	7100 ± 540

## 4. Discussion

With each new eruption, our understanding of the outburst mechanism of RS Oph steadily improves, thanks to ever more accurate data and comparison to previous events. Thanks to the radio imaging of the 2021 eruption presented in this paper we are now able to characterize in great detail the evolving morphology of the expanding bipolar ejecta, and determine the physical conditions of the surrounding medium in which they propagate.

### 4.1. The evolving source morphology

From the high-resolution radio observations presented in this work we find an expanding source structure consisting of three main components: a central and compact core region, located within a few mas from the *Gaia* DR3 position (Gaia Collaboration et al. 2016, 2023), and two expanding lobes in east-west direction, on opposite sides from the central binary. This evolving source structure is notably consistent with the images at similar frequencies for the past RS Oph nova event in 2006 reported by O’Brien et al. (2006); Rupen et al. (2008); Sokoloski et al. (2008). However, thanks to the accurate astrometric position provided by the *Gaia* DR3 position, the key improvement from the 2021 data is the realisation that the ring-like structure at early times is actually the western lobe, as the binary system is located just to the east of this. This provides firm support for the

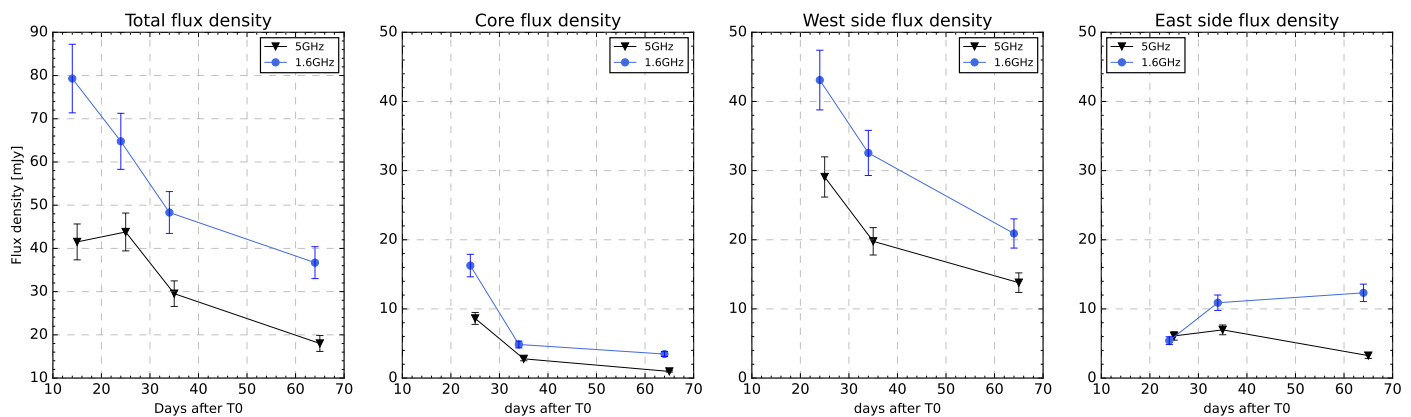


**Fig. 4.** Light-curves at 1.6 GHz (blue circles) and 5 GHz (black triangles) for the whole source (first frame), the core (second frame), the western lobe (third frame) and the eastern lobe (fourth frame). All values are reported in Table 3.

**Table 3.** Flux densities of the different source regions.

		Epoch I mJy	Epoch II mJy	Epoch III mJy	Epoch V mJy
5 GHz	Total	$41.5 \pm 4.2$	$43.8 \pm 4.4$	$29.5 \pm 3.0$	$18.0 \pm 1.8$
	Core	-	$8.6 \pm 0.9$	$2.8 \pm 0.3$	$1.0 \pm 0.1$
	East	-	$6.1 \pm 0.6$	$7.0 \pm 0.7$	$3.2 \pm 0.4$
	West	-	$29.1 \pm 2.9$	$19.8 \pm 2.0$	$13.8 \pm 1.4$
1.6 GHz	Total	$79.3 \pm 7.9$	$64.8 \pm 6.5$	$48.3 \pm 4.8$	$36.7 \pm 3.7$
	Core	-	$16.3 \pm 1.6$	$4.9 \pm 0.5$	$3.5 \pm 0.4$
	East	-	$5.4 \pm 0.6$	$10.9 \pm 1.1$	$12.3 \pm 1.3$
	West	-	$43.1 \pm 4.3$	$32.6 \pm 3.3$	$20.9 \pm 2.1$

bipolar outflow expansion scenario. Furthermore, as we argued in Munari et al. (2022), the images obtained from this observing campaign clearly reveal that the gravitational pull of the WD channels most of the mass lost by the RG towards the orbital plane and forms the so-called DEOP. The confinement of the ejected material into the two observed bipolar outflow is produced by the combined effect of the DEOP and the accretion disk around the WD (e.g. Orlando & Drake 2012). Within this scenario, the western side represents the approaching lobe that is located in the foreground to the DEOP, while the eastern side represents the receding lobe expanding behind the DEOP.

In more detail, this is the evolution process that we can infer from the images presented in Fig. 1. During the first epoch (14–15 days after  $T_0$ ), at both 1.6 and 5 GHz, we only see the approaching western lobe, projected on the plane of the sky, with emission from the central region absorbed by the dense and ionized gas and the western lobe laying in front. Similarly, the eastern lobe is completely hidden from view by absorption from the densest and ionized inner regions of DEOP. As the western lobe further propagates with a circular shape, during epoch II (24–25 days from  $T_0$ ) the central core emerges with a bright and compact structure, and a brightness temperature of the order of  $7 \times 10^8$  K at 5 GHz and  $4 \times 10^8$  K at 1.6 GHz, indicating the non-thermal nature for the emission. A non-thermal origin for the whole radio emission on these scales<sup>2</sup> is also indicated by the spectral properties: the integrated spectral index in the core region and the

western lobe are negative, with average values of  $-0.50 \pm 0.12$  and  $-0.40 \pm 0.12$ , respectively; the eastern lobe has a slightly positive spectral index ( $0.10 \pm 0.13$ ), explained by the fact that as the eastern lobe leading edge emerges behind the DEOP, it is clearly visible at 5 GHz while at 1.6 GHz the free-free absorption effect is still significant (the optical depth going like  $\tau_\nu \propto \nu^{-2.1}$ ) and its emission is still opaque. We note that the source extension and morphology during epoch II (24–25 days from  $T_0$ ) are in good agreement with the results about the 2006 outburst reported by Rupen et al. (2008) (20.8 and 26.8 days after the outburst) and O’Brien et al. (2006) (21.5 and 28.7 days after the outburst), obtained with the VLBA at 1.7 and 5 GHz.

During the following two epochs we can track the expanding source structure, that reaches an overall east-west extension of  $\sim 200$  mas ( $\sim 540$  AU) during the last observing epoch (64–65 days after  $T_0$ ). As the source structure expands and gets more diffuse it also becomes fainter, showing an overall decreasing flux density trend with time, both for the core region and the western lobe. On the other hand, the flux density of the eastern lobe shows an increasing trend as it gradually emerges behind the DEOP (see Fig. 4). We note that in this last epoch the core flux density has dropped by  $\sim 80\%$ , and the brightest source region is found in the western lobe edge, that maintains a less steep spectral index of  $-0.36 \pm 0.13$ . On the other hand, both the core region and the eastern lobe become more transparent with spectral indexes of  $-1.13 \pm 0.13$  and  $-1.17 \pm 0.12$ , respectively. We note that during the last observing epoch the core brightness temperature decreases as well, down to values of  $3.0 \times 10^5$  K at 5 GHz and  $5.0 \times 10^6$  K at 1.6 GHz, indicating how the deceleration of the ejecta close to the equatorial plane and therefore the densest regions of DEOP is almost completed. The 1.6 GHz images during epochs III (35 days after  $T_0$ ) and V (65 days after  $T_0$ ) are consistent with the images reported by Sokolowski et al. (2008) obtained from 34 to 51 days after the 2006 outburst.

As it emerges from the analysis of the angular separation with time of the two lobes (see Fig. 3) during the  $14 \leq (T - T_0) \leq 65$  day interval probed by our observations, the overall evolving source structure is consistent with a linear expansion, with no hints of significant deceleration of eastern and western lobes expanding perpendicular to the orbital plane. This is an indication that the density gradient perpendicular to the orbital plane is very steep, with no mass higher than 50 AU above the equatorial plane and probably confined much closer to the plane than this upper limit.

<sup>2</sup> The analysis of the source structure evolution on larger scales, by means of multi-frequency e-MERLIN and Jansky Very Large Array observations, will be presented in a separate work (Williams et al. in prep.).

#### 4.2. Density profile and total mass of DEOP

If we assume intrinsic similarity and symmetry at any of the observing epochs between the two expanding lobes, the flux ratio between the western lobe seen in foreground and the eastern lobe seen through the absorbing DEOP allows to estimate the radial dependence of density along the DEOP.

To this aim we adopt the following expression for the free-free optical thickness of ionized gas (Mezger & Henderson 1967; Condon & Ransom 2016):

$$\tau_\nu \approx 3.28 \times 10^{-7} \left( \frac{T}{10^4} \right)^{-1.35} \nu^{-2.1} n_e^2 s \quad (2)$$

with the temperature  $T$  in Kelvin, the frequency  $\nu$  in GHz, the electron density  $n_e$  in  $\text{cm}^{-3}$ , the geometrical thickness  $s$  in pc, and assuming the same number of electrons and ions  $n_e n_i \approx n_e^2$ .

Being interested in the order of magnitude of the derived density, we consider the DEOP as being approximated by a plane-parallel slab of total  $s$  thickness constant through the radial extent, with an electron density  $n_e$  dependent only from the radial distance and otherwise constant in the height direction. Considering that the nuclear burning at the surface of the WD continued uninterrupted to day +82, i.e. well past our latest radio observation (Munari & Valisa 2022; Page et al. 2022), we assume full ionization within DEOP over its radial extent explored by our radio observations. In the previous section we estimated that by an height of 50 AU above the equatorial plane, the density within the DEOP has dropped to negligible values; assuming the drop to be exponential with height (i.e.  $\rho(z) \propto \rho(0)e^{-z/z_0}$ ), the accumulated column density is equivalent to the case of constant density over an height  $\leq 12$  AU. Accordingly, we adopt  $s=20$  AU in Eq.(2). Finally, for de-projection purposes, we adopt the orbital inclination of  $i=54^\circ$  derived by Munari et al. (2022).

From Fig. 1 and its comparison with equivalent mapping of the 2006 eruption by Rupen et al. (2008), the earliest appearance of the extincted eastern lobe occurred at 5 GHz on day +20 at an angular distance of  $\sim 25$  mas from the position of RS Oph, corresponding to a de-projected distance of  $\sim 50$  AU. Taking a brightness ratio 100 at this epoch for the western lobe with respect to the eastern one, the electron density results in  $n_e(50 \text{ AU})=2.0 \times 10^6 \text{ cm}^{-3}$ . At the time of the latest radio epoch on day +65, the brightness ratio at 5GHz has reduced to 4 for the apex of the lobes located at  $\sim 87$  mas from RS Oph, corresponding to a de-projected distance of  $\sim 175$  AU from central binary, resulting in an electron density of  $n_e(175 \text{ AU})=3.8 \times 10^5 \text{ cm}^{-3}$ .

An estimate of the electron density at the DEOP inner regions can be obtained from the recombination time following the initial UV-flash at the very start of the outburst, for which Munari & Valisa, (2021) derived  $n_e=1.1 \times 10^7 \text{ cm}^{-3}$ .

There is therefore a clear evidence of a radial dependence of the density going from  $1.1 \times 10^7 \text{ cm}^{-3}$  close to the central binary, to  $2.0 \times 10^6$  at 50 AU distance, and to  $3.8 \times 10^5 \text{ cm}^{-3}$  at 175 AU. The behavior is summarized in Fig. 6 where the fitting curve represents the relation  $\rho(r) \propto r^{-1.25}$ . Integrating the density along the DEOP volume between  $10 \leq r \leq 175$  AU leads to a total DEOP mass of  $M_{\text{DEOP}} = 4.3 \times 10^{-6} M_\odot$ .

Supposing the RG loses mass via a wind at a typical speed of  $20 \text{ km s}^{-1}$  and that the vast majority of the mass lost ends up in the DEOP, the required RG mass-loss rate is  $\dot{M}_{\text{RG}} = 1 \times 10^{-7} M_\odot/\text{yr}$ , which compares well with standard estimates (eg. Livio & Warner 1984), arguing in favor of the general soundness of the above reasoning.

To power an outburst every  $\sim 20$  yrs, the WD in RS Oph has to be massive and accrete at a high rate. Theoretical models by

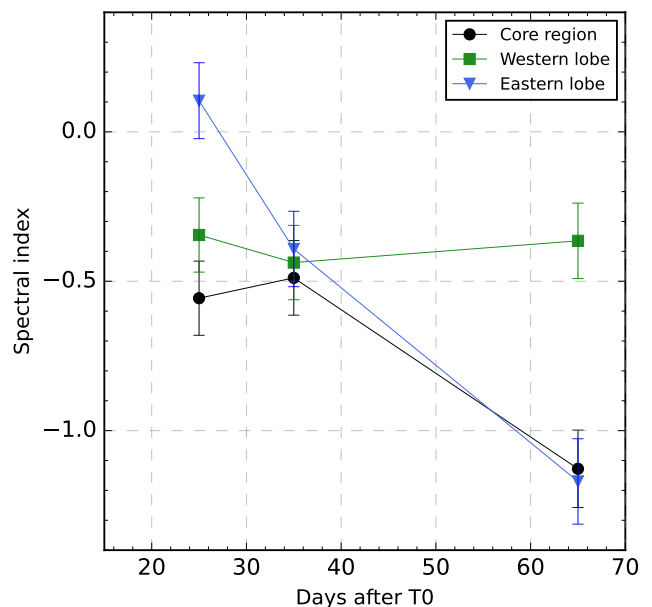


**Fig. 5.** 1.6 - 5 GHz spectral index for the core region (black circles), western lobe (green squares) and eastern lobe (blue triangles). All values are reported in Table 4.

**Table 4.** Spectral index values for the different source regions.

Spectral index	Epoch II	Epoch III	Epoch V
Core	$-0.56 \pm 0.12$	$-0.49 \pm 0.12$	$-1.13 \pm 0.13$
East	$0.10 \pm 0.13$	$-0.39 \pm 0.13$	$-1.17 \pm 0.14$
West	$-0.35 \pm 0.12$	$-0.44 \pm 0.12$	$-0.36 \pm 0.13$

Yaron et al. (2005) require accretion rates  $\dot{M}_{\text{WD}} > 10^{-8} M_\odot \text{ yr}^{-1}$  for a  $1.4 M_\odot$  WD, and  $\dot{M}_{\text{WD}} > 10^{-7} M_\odot \text{ yr}^{-1}$  if the mass of the WD reduces to  $1.25 M_\odot$ . These estimates are in good agreement with the results of X-ray observations of RS Oph in quiescence reported by Nelson et al. (2011), that have placed an upper limit of  $\dot{M}_{\text{WD}} < 2 \times 10^{-8} M_\odot \text{ yr}^{-1}$  for RS Oph. Comparing with our estimate for the RG mass loss of  $\dot{M}_{\text{RG}} = 1 \times 10^{-7} M_\odot/\text{yr}$ , it is interesting to conclude that the WD in RS Oph is likely accreting around one tenth of the mass lost by the RG and that the great majority therefore goes to feed the circumstellar region, and the DEOP in particular. This also has implications for the mass-reservoir constituted by the RG to keep powering new eruptions on the WD and, pending the mass-gain efficiency of eruption, the ultimate fate of the WD itself.

#### 4.3. High-resolution source morphology

The full resolution image at 5 GHz for epoch I (14 days after  $T_0$ ) reveals a complex, granular-like, source morphology (see Fig. 2). Considering that during this epoch the total extension in the north-south direction is  $\sim 30$  mas, we obtain a transverse expansion speed of  $\sim 0.02$ .

A similar elongated source morphology was found with the VLBA, at 5 GHz, 14 days after the 2006 outburst by O'Brien et al. (2008). The position, shape and size of the brightness distribution best-fit ellipse reported in O'Brien et al. (2008), are in good agreement with the total intensity source structure that we find 14 days after the 2021 outburst (gray dots in Fig. 2). This

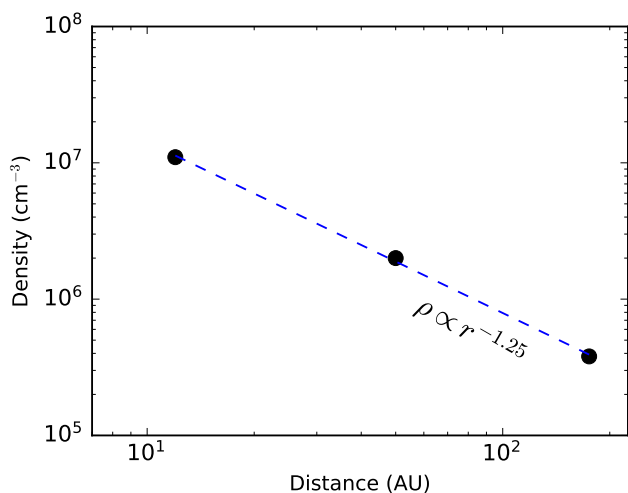


**Fig. 6.** Dependence on radial distance from the central binary of the electron density within DEOP.

supports the idea that the way in which the RG wind refills the circumstellar space - which has been emptied by the expanding ejecta of the previous nova eruption - replicates self-similar at each new event, as the evolution at optical wavelengths of each outburst is identical to all others.

A marked granular structure, although at a much closer distance to the WD, is supported by the X-ray observations at the onset of the supersoft phase during the 2006 outburst of RS Oph (Osborne et al. 2011), and to a lower degree also during the 2011 event (Page et al. 2022). Our EVN observations suggest that such granularity is present also to scales much larger than implied by the X-ray observations. It is beyond the goals of this paper to investigate the origin of such a clumpy structuring of the ejecta and of the circumstellar medium around RS Oph, but various mechanisms may be at work at different distances from the central binary, involving inhomogeneities in the wind blowing off the WD during the burning phase as well as the turbulent nature of shocks propagating through the pre-existing (and probably itself clumpy) slow circumstellar material.

## 5. Conclusions

In this work we present the results of a high-resolution VLBI radio monitoring of the recurrent and symbiotic nova RS Oph after the most recent outburst occurred during august 2021. By means of multi-epoch EVN + e-MERLIN observations at 1.6 and 5 GHz, from 14 to 65 days after the explosion, we characterize in great detail the evolving source morphology and the physical conditions of the surrounding medium in which the ejected material propagates.

At both frequencies we identify a triple-component source morphology, with a compact central core region and two elongated bipolar outflow expanding linearly in east-west direction, with an average speed of  $\sim 7000 \text{ km s}^{-1}$ . We estimate a total mass of  $4.3 \times 10^{-6} M_{\odot}$  for the DEOP, representing the density enhancement above the orbital plane that we reveal in our images as a flux density depression between the eastern lobe and the rest of the source. We find a clear radial dependence of the density within the DEOP, that varies from  $1.1 \times 10^7 \text{ cm}^{-3}$  in the near vicinity of the central binary to  $8 \times 10^5 \text{ cm}^{-3}$  at  $\sim 175 \text{ AU}$ . Based on our results, we can firmly conclude that the majority

of the mass lost by the RG companion ends up in the DEOP and the circumstellar region, with only about one-tenth of it being accreted by the WD.

*Acknowledgements.* The European VLBI Network is a joint facility of independent European, African, Asian, and North American radio astronomy institutes. Scientific results from data presented in this publication are derived from the following EVN project code: RG012. The research leading to these results has received funding from the European Union's Horizon 2020 Research and Innovation Programme under grant agreement No. 101004719 (OPTICON RadioNet Pilot). e-MERLIN is a National Facility operated by the University of Manchester at Jodrell Bank Observatory on behalf of STFC. This work has made use of data from the European Space Agency (ESA) mission *Gaia* (<https://www.cosmos.esa.int/gaia>), processed by the *Gaia* Data Processing and Analysis Consortium (DPAC, <https://www.cosmos.esa.int/web/gaia/dpac/consortium>). Funding for the DPAC has been provided by national institutions, in particular the institutions participating in the *Gaia* Multilateral Agreement. RL, MG, UM acknowledge financial support from INAF 2022 fundamental research programme ob. fun. 1.05.12.05.16. BM acknowledges financial support from the State Agency for Research of the Spanish Ministry of Science and Innovation under grant PID2019-105510GB-C31/AEI/10.13039/501100011033 and through the Unit of Excellence María de Maeztu 2020–2023 award to the Institute of Cosmos Sciences (CEX2019-000918-M).

## References

- Acciari V. A., Ansoldi S., Antonelli L. A., Arbet Engels A., Artero M., Asano K., Baack D., et al., 2022, *NatAs*, 6, 689.
- Azzollini A., Shore S. N., Kuin P., Page K. L., 2023, *A&A*, 674, A139.
- Brandi, E., Quiroga, C., Mikołajewska, J., et al. 2009, *A&A*, 497, 815.
- Cheung, C. C., Johnson, T. J., Jean, P., et al. 2022, *ApJ*, 935, 44.
- Chomiuk L., Linford J. D., Yang J., O'Brien T. J., Paragi Z., Mioduszewski A. J., Beswick R. J., et al., 2014, *Natur*, 514, 339.
- Condon, J. J. & Ransom, S. M. 2016, *Essential Radio Astronomy*. ISBN: 978-0-691-13779-7. Princeton, NJ: Princeton University Press, 2016.
- Das R., Banerjee D. P. K., Ashok N. M., 2006, *ApJL*, 653, L141.
- de Ruiter I., Nyamai M. M., Rowlinson A., Wijers R. A. M. J., O'Brien T. J., Williams D. R. A., Woudt P., 2023, *MNRAS*, 523, 132.
- Eyres S. P. S., O'Brien T. J., Beswick R., Muxlow T. W. B., Anupama G. C., Kantharia N. G., Bode M. F., et al., 2009, *MNRAS*, 395, 1533.
- Gaia Collaboration, Prusti T., de Bruijne J. H. J., Brown A. G. A., Vallenari A., Babusiaux C., Bailer-Jones C. A. L., et al., 2016, *A&A*, 595, A1.
- Gaia Collaboration, Vallenari A., Brown A. G. A., Prusti T., de Bruijne J. H. J., Arenou F., Babusiaux C., et al., 2023, *A&A*, 674, A1.
- Giroletti, M., Munari, U., Körding, E., et al. 2020, *A&A*, 638, A130.
- Giroletti, M., Munari, U., Marcote, B., et al. 2023, 15th European VLBI Network Mini-Symposium and Users' Meeting, PoS(EVN2022)038
- Greisen, E. W. 2003, *Information Handling in Astronomy - Historical Vistas*, 285, 109.
- Islam N., Mukai K., Sokolowski J. L., 2024, *ApJ*, 960, 125.
- H. E. S. S. Collaboration, Aharonian, F., Ait Benkhali, F., et al. 2022, *Science*, 376, 77.
- Högbom, J. A. 1974, *A&AS*, 15, 417
- Keimpema, A., Kettenis, M. M., Pogrebenko, S. V., et al. 2015, *Experimental Astronomy*, 39, 259.
- Kettenis, M., van Langevelde, H. J., Reynolds, C., et al. 2006, *Astronomical Data Analysis Software and Systems XV*, 351, 497
- Lico, R., Giroletti, M., Orienti, M., et al. 2012, *A&A*, 545, A117.
- Livio M., Warner B., 1984, *Obs*, 104, 152
- Mezger, P. G. & Henderson, A. P. 1967, *ApJ*, 147, 471.
- Molaro P., Izzo L., Selvelli P., Bonifacio P., Aydi E., Cescutti G., Guido E., et al., 2023, *MNRAS*, 518, 2614. doi:10.1093/mnras/stac2708
- Munari, U. & Valisa, P. 2021, arXiv:2109.01101.
- Munari U., Valisa P., 2021, *ATel*, 14860
- Munari, U. & Valisa, P. 2022, arXiv:2203.01378.
- Munari U., Tabacco F., 2022, *RNAAS*, 6, 103.
- Munari, U., Giroletti, M., Marcote, B., et al. 2022, *A&A*, 666, L6.
- Nayana A. J., Anupama G. C., Roy N., Banerjee D. P. K., Singh K. P., Sonith L. S., Kamath U. S., 2024, *MNRAS*, 528, 5528.
- Nelson T., Mukai K., Orio M., Luna G. J. M., Sokolowski J. L., 2011, *ApJ*, 737, 7.
- Ness J.-U., Beardmore A. P., Bode M. F., Darnley M. J., Dobrotka A., Drake J. J., Magdolen J., et al., 2023, *A&A*, 670, A131.
- O'Brien, T. J., Bode, M. F., Porcas, R. W., et al. 2006, *Nature*, 442, 279.
- O'Brien, T. J., Beswick, R. J., Bode, M. F., et al. 2008, *ASPC* 401, 239
- Orio M., Gendreau K., Giese M., Luna G. J. M., Magdolen J., Strohmayer T. E., Zhang A. E., et al., 2023, *ApJ*, 955, 37.
- Orlando, S. & Drake, J. J. 2012, *MNRAS*, 419, 2329.



- Osborne J. P., Page K. L., Beardmore A. P., Bode M. F., Goad M. R., O'Brien T. J., Starrfield S., et al., 2011, *ApJ*, 727, 124.
- Page, K. L., Beardmore, A. P., Osborne, J. P., et al. 2022, *MNRAS*, 514, 1557.
- Pandey R., Habtie G. R., Bandyopadhyay R., Das R., Teyssier F., Guarro Fló J., 2022, *MNRAS*, 515, 4655.
- Rupen M. P., Mioduszewski A. J., Sokoloski J. L., 2008, *ApJ*, 688, 559.
- Shepherd, M. C. 1997, *Astronomical Data Analysis Software and Systems VI*, 125, 77.
- Shidatsu, M., Negoro, H., Mihara, T., et al. 2021, *The Astronomer's Telegram*, 14846.
- Sokoloski, J. L., Rupen, M. P., & Mioduszewski, A. J. 2008, *ApJ*, 685, L137.
- Sokolovsky, K., Aydi, E., Chomiuk, L., et al. 2021, *The Astronomer's Telegram*, 14886.
- Tingay, S. J., Murphy, D. W., Lovell, J. E. J., et al. 1998, *ApJ*, 497, 594
- Tomov N. A., Tomova M. T., Stoyanov K. A., Bonev T. R., Zamanov R. K., Iliev I. K., Nikolov Y. M., et al., 2023, *A&A*, 671, A49.
- Zamanov R., Marchev V., Marchev D., Atanasova T., Pavlova N., 2022, *ATel*, 15330
- Yaron O., Prialnik D., Shara M. M., Kovetz A., 2005, *ApJ*, 623, 398.
- Williams, D., O'Brien, T., Woudt, P., et al. 2021, *The Astronomer's Telegram*, 14849.
- Woodward, C. E., Evans, A., Banerjee, D. P. K., et al. 2021, *The Astronomer's Telegram*, 14866.